Avestia Publishing
Journal of Fluid Flow, Heat and Mass Transfer (JFFHMT)
Volume 12, Year 2025
ISSN: 2368-6111
DOI: 10.11159/jffhmt.2025.002

Effect of Heat Transfer Coefficients in Forced Convective Cooling of Batteries on the Sustained Performance of PCMs

Vanita A. Wagh, Sandip K. Saha
Indian Institute of Technology Bombay, Department of Mechanical Engineering
Powai, Mumbai-400076, India
214100027@iitb.ac.in; sandip.saha@iitb.ac.in

Abstract - *Effective thermal management of lithium-ion batteries (LIBs) is necessary to sustain phase stability in an optimal temperature range of 15 to 45 °C, which ensures longevity and prevents thermal runaway under repeated high-frequency discharging-charging cycles. This study focuses on determining the optimal heat transfer coefficient (h) required to facilitate complete solidification during the charging after the full melting of phase change materials (PCMs) during high-rate discharging for effective and continuous use of PCMs. Utilizing the Newman-Tiedemann-Gu-Kim (NTGK) model, the performance of the SAMSUNG ICR 18650-26J battery is studied. The cell is encased by a copper shell, followed by the addition of the PCM, and then further encapsulated by another copper shell. The present study evaluated three PCMs such as n-Heneicosane, OM42, and n-Docosane and a range of heat transfer coefficients (h) from 20 W/m²·K to 500 W/m²·K for the thermal management of cells. It is found that increasing the PCM thickness from 3 mm to 4 mm reduces the maximum cell temperature from 53.19 °C to 51.94 °C during a 5C discharge at 40 °C ambient temperature, however, resulting in lower PCM utilization, making 3 mm as the optimal PCM thickness. At an ambient temperature of 35 °C, n-Heneicosane remains in the liquid state, whereas n-Docosane maintained better thermal regulation and complete solidification, demonstrating its suitability for moderate ambient conditions. Under harsh conditions (40°C), increasing the convective heat transfer coefficient to 500 W/m²·K during charging allows n-Docosane to solidify within 750 s fully, ensuring effective thermal management.*

***Keywords*:** Lithium-ion batteries, Phase change materials, NTGK model, Discharging-charging cycles.

Nomenclature

A	Porosity function
C	Specific heat capacity (J/kg·K)
d	Diameter (m)
f_l	Liquid fraction
g	Acceleration due to gravity (m/s²)
E	Total enthalpy (J/kg)
e	Sensible heat (J/kg)
ΔE	Enthalpy change (J/kg)
H	Height (m)
h	Heat transfer coefficient (W/m²·K)
j	Volumetric rate of current transfer (A)
k	Thermal conductivity (W/m·K)
L	Latent heat (J/kg)
l	Length (m)
$\dot{q}$	Volumetric heat generation rate (W/m³)
r	Radius (m)
S_h	Enthalpy source term
S_u	Momentum source term
T	Temperature (K)
t	Time (s)
t_h	Thickness (m)
$\vec{V}$	Velocity (m/s)
v	Mean fluid velocity (m/s)
Vol	Volume (m³)

Greek Symbols

ρ	Density (kg/m³)
σ_+	Electric conductivity for positive electrode (Ω⁻¹)
σ_-	Electric conductivity for negative electrode (Ω⁻¹)
ϕ_+	Phase potentials for positive electrodes (V)
ϕ_-	Phase potentials for negative electrodes (V)
μ	Dynamic fluid viscosity (N.s/m²)
β	Thermal expansion coefficient (K⁻¹)

Date Received: 2024-08-28
Date Revised: 2024-12-16
Date Accepted: 2025-01-20
Date Published: 2025-01-30

Subscripts

a	Ambient
B	Battery
cell	Battery
Cu	Copper
ECh	Electrochemical
i	Inner layer of copper
m	Melting
nom	Nominal
o	Outer layer of copper
p	Phase change material
ref	Reference
short	Internal short circuit

1. Introduction

Road transportation significantly contributes to global greenhouse gas emissions, accounting for about 72% of the transportation sector's emissions [1]. In some regions, it is responsible for 85.2% of CO_2 emissions [2]. Emissions from conventional road transport not only increase greenhouse gases but also deteriorate air quality, particularly in urban areas, through pollutants like CO_2, sulfur dioxide (SO_2), and nitrogen oxides (NO_x) [3]. The urgent need to address environmental concerns, particularly greenhouse gas emissions and air pollution, has shifted research priorities towards greener alternatives such as battery electric vehicles (EVs). Factors influencing the diffusion of EVs in urban areas are being studied intensively [1], emphasizing the importance of transitioning to cleaner transportation options to address environmental challenges effectively. In this context, lithium-ion batteries' high specific power, specific energy, long lifespan, and compact size and weight make them suitable for the high-energy storage demands of EVs.

Lithium-ion batteries have seen significant advancements, enhancing their adaptability in electric vehicles (EVs) and other applications. Key improvements include the development of high-capacity cathode materials, which increase energy density for EV use [2]. Research has also focused on integrating lithium-ion batteries with technologies like perovskite solar cells to enhance performance and charging capabilities [3]. Additionally, the development of lithium-free transition metal monoxides for positive electrodes has improved energy/power density, reduced costs, and extended cycle life, which is critical for EVs and large-scale energy storage [4].

In addressing thermal management challenges in battery systems, phase change materials (PCMs) have been increasingly incorporated into Battery Thermal Management Systems (BTMS). The advantages of using PCMs include enhanced thermal regulation, improved energy efficiency, and reduced system complexity. By utilizing PCMs in BTMS, the heat generated during battery operation is absorbed by the PCM as it changes its phase from solid to liquid, effectively storing and dissipating heat. This process helps to maintain the battery temperature within a safe operating range, preventing overheating and ensuring optimal performance. Karmkar et al. [5] demonstrated that PCMs possess high latent heat capacities, enabling them to absorb and release significant amounts of energy during phase transitions. This property makes PCMs highly effective for managing thermal fluctuations in battery systems. Song et al. [6] demonstrated that compared to traditional cooling methods, PCMs offer passive thermal management, eliminating the need for active cooling components like fans or pumps, which can consume additional energy and add complexity to the system. Zhang et al. [7] highlighted that PCMs provide more uniform temperature distribution within the battery pack, reducing hotspots and enhancing overall system reliability. In conclusion, integrating phase change materials into battery thermal management systems offers a sustainable and effective solution to address thermal challenges, providing efficient heat dissipation, improved energy efficiency, and enhanced system reliability compared to traditional cooling methods.

The thermal management of lithium-ion batteries encased with PCMs is crucial for their performance and safety during high-rate discharging and charging cycles. A higher heat transfer coefficient aids in efficient heat dissipation, managing the heat generated during rapid charging and discharging processes. This allows for quick heat transfer to the PCM, enabling effective absorption and storage of excess heat, thus maintaining the battery temperature within a safe operating range. Wagh et al. [8] found that incorporating fins in the PCM can enhance heat dissipation capacity by improving heat transfer. Li et al. [9] discussed using different PCMs, such as RT15, RT31, EG5, and EG26, which have been experimentally investigated to enhance heat transfer rates and the overall thermal performance of electric vehicle battery packs. Angani et al. [10] highlighted that integrating PCMs in battery packs had improved heat transfer rates and thermal performance under extreme temperature conditions, contributing to better thermal regulation and safety of the battery system. Talluri et al. [11] also supported these findings by showing the

benefits of PCMs in maintaining optimal battery temperatures. However, despite these advancements, a significant research gap remains in understanding the specific heat transfer coefficients required for the complete solidification of PCMs during continuous high-rate discharging-charging cycles.

While various PCMs have been studied, n-Heneicosane, OM42, and n-Docosane are selected for this study due to their specific melting temperatures (43.6 °C, 43 °C, and 44.7 °C, respectively), which closely align with India's ambient temperature conditions. This makes them particularly suitable for thermal management in environments with similar climatic characteristics. This research evaluates these PCMs in managing the thermal behaviour of SAMSUNG ICR 18650-26J Lithium-ion battery, focusing on maintaining battery temperatures within the crucial range of 15 °C to 45 °C during high-rate discharging and charging cycles [12]. This study systematically analyzes the thermal behavior of a high discharge rate (5C) configuration combined with charging rates (1C) while investigating heat transfer coefficients ranging from 20 W/m^2·K to 500 W/m^2·K to identify optimal values for maintaining safe battery temperatures and ensuring complete PCM solidification during continuous high-rate cycles under harsh ambient conditions. By examining specific PCMs and heat transfer coefficients, the study aims to enhance battery safety and performance under high C-rate cycles. The findings provide new insights into the critical heat transfer coefficients for PCM solidification, offering valuable data on PCM effectiveness in specific configurations. This research provides essential insights for optimizing thermal management systems in LIBs for EVs, enhancing performance and safety.

2. Methodology

2.1. Battery and PCM Selection with Numerical Analysis Setup

The study utilizes a SAMSUNG ICR 18650-26J Lithium-ion battery with a nominal capacity of 2600 mAh. Figure 1 illustrates the battery structure, which includes an 18 mm diameter core encased by a 0.5 mm thick inner copper shell. This core-shell assembly is then surrounded by a 3 mm layer of PCM and further protected by a 0.5 mm outer copper shell. Additionally, both the top and bottom of the battery are fitted with 1 mm thick caps. Table 1 details the battery's operating parameters, while Table 2 lists material properties, such as thermal conductivity, that affect heat dissipation in lithium-ion batteries.

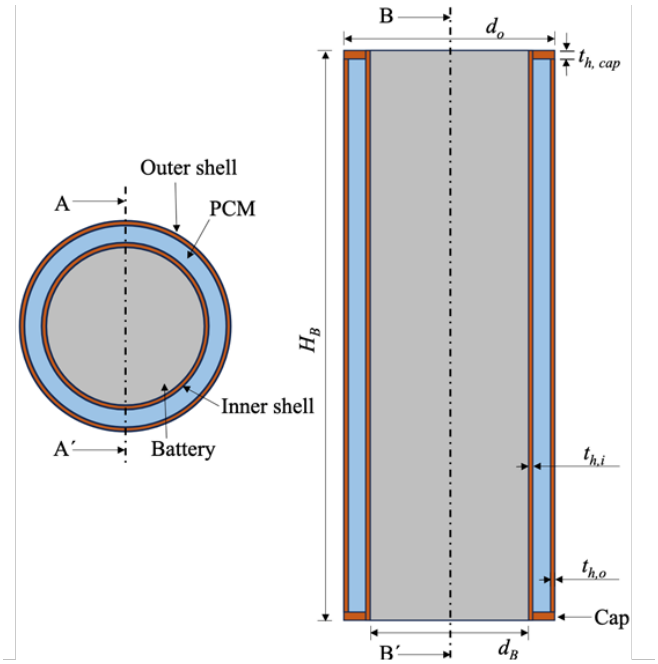

Figure 1. Battery encased with copper shells and PCM.

Table 1. Specifications of Samsung 18650 battery [8]

Parameter	Value
Nominal voltage (V)	3.7
Minimum stop voltage (V)	2.8
Maximum stop voltage (V)	4.2
Cell weight (g)	43.87
Nominal capacity (mAh)	2600
Electrolyte type	Carbonate based
Cathode type	Lithium Cobalt Oxide
Anode type	Graphite
Diameter of the cell (mm)	18
Height of the cell (mm)	65

Table 2. Thermophysical properties of lithium-ion battery [8]

Property	Value
Specific heat of positive tab (J/kg·K)	871
Density of positive tab (kg/m^3)	2719
Thermal conductivity for positive tab (W/m·K)	202
Specific heat of negative tab (J/kg·K)	381
Density of negative tab (kg/m^3)	8978
Thermal conductivity for negative tab (W/m·K)	387.6
Thermal conductivity of cell: radial, tangential, axial (W/m·K)	3.4, 24, 24

The selected PCMs, n-Heneicosane, OM42, and n-Docosane, are chosen for their melting points and

thermal properties, optimal for maintaining battery temperature during high-rate discharging and charging cycle of 5C-1C configuration. The performance of battery-PCM configuration is examined under heat transfer coefficients ranging from 20 to 500 W/m²·K. The specifications and properties of the battery can be found in [13]. The thermophysical properties of PCMs are listed in Table 3.

Table 3. Thermophysical properties of n-Docosane [14], n-Heneicosane and OM42

Property	n-Docosane	n-Heneicosane	OM42
ρ (kg/m^3)	778	772	865
T_{ref} (°C)	42.1	39.2	43
β (K^{-1})	1×10^{-3}	1×10^{-3}	1×10^{-3}
k (W/m·K)	0.21	0.145	0.19
T_m (°C)	44.7	43.6	43
L (J/kg)	257000	294600	183000
C (J/kg·K)	2650	2386	2710
μ (kg/m·s)	0.0039	0.0033	0.0039

2.2. Numerical Model and Simulation

The thermal performance of the battery is simulated using the Newman-Tiedemann-Gu-Kim (NTGK) model. The governing equations for the thermal and electrical energy conservation within the battery are solved using a Multi-Scale Multi-Domain (MSMD) approach [8]. The governing equations for current flux at both the positive and negative electrodes are detailed as [15], [16].

$$\frac{\partial(\rho_B c_B T_B)}{\partial t} = \nabla\cdot\left(K_B \nabla T_B\right) + \sigma_+|\nabla\phi_+|^2 + \sigma_-|\nabla\phi_-|^2 + \dot{q}_{ECh} + \dot{q}_{short} \quad (1)$$

$$\nabla\cdot(\sigma_+\nabla\phi_+) = -(j_{ECh} - j_{short}) \quad (2)$$

$$\nabla\cdot(\sigma_-\nabla\phi_-) = (j_{ECh} - j_{short}) \quad (3)$$

The enthalpy method is employed to model the solidification and melting of the PCM. The fluid flow of the PCM is assumed to be laminar and Newtonian, with constant property values across the temperature range considered in the study. The governing equations that describe the PCM domain are presented below:

Conservation of Mass:

$$\frac{\partial\rho_p}{\partial t} + \nabla.\left(\rho_p\vec{V}\right) = 0 \quad (4)$$

Conservation of Momentum:

$$\left(\frac{\partial}{\partial t} + \nabla.\vec{V}\right)\left(\rho_p\vec{V}\right) = -\nabla P + \nabla.\left(\mu\nabla\vec{V}\right) + S_u + \frac{\rho_p g\beta(e - e_{ref})}{c_p} \quad (5)$$

Conservation of Energy:

$$\frac{\partial(\rho_p c_p T)}{\partial t} + \nabla.\left(\rho_p\vec{V}c_p T\right) = \nabla.\left(k_p\nabla T\right) + S_h \quad (6)$$

where the velocity vector, $\vec{V} = u\hat{\imath} + v\hat{\jmath} + w\hat{k}$. The source term S_u is used to model fluid flow during phase change. β is a thermal expansion coefficient and e_{ref} is a reference value of the sensible heat. S_h is a phase related source term. The liquid fraction of PCM is expressed as,

$$f_l = \frac{\Delta E}{L} \quad (7)$$

The initial temperature of the battery and PCM is set to the ambient temperature of 40 °C. The PCM is initially in a solid phase, and the velocity field is set to zero.

$$\text{At } t = 0;\ T(x,y,z) = T_a = 40\ °C \text{ and } \vec{V} = 0, \quad (8)$$

Based on Newton's law of cooling, the boundary condition on the external housing surface is given as:

$$k_{cu}\frac{\partial T_{cu,o}}{\partial r} = h(T_{cu,o} - T_a) \quad (9)$$

At the interface between the battery and the inner copper shell surface:

$$-k_B\frac{\partial T_B}{\partial r} = -k_{cu}\frac{\partial T_{cu,i}}{\partial r};\ T_B = T_{cu,i} \quad (10)$$

At the interface between the PCM and the inner copper surface, the boundary condition is described by:

$$r = \frac{d_B}{2} + t_{h,cu,i};\ -k_{cu}\frac{\partial T_{cu,i}}{\partial r} = -k_p\frac{\partial T_p}{\partial r};\ T_{cu,i} = T_p \quad (11)$$

Similarly, at the interface between the PCM and the outer copper surface, the boundary condition is given as:

$$r = \frac{d_B}{2} + t_{h,\,cu,i} + t_p;\ -k_p\frac{\partial T_p}{\partial r} = -k_{cu}\frac{\partial T_{cu,o}}{\partial r};\ T_p = T_{cu,o} \quad (12)$$

The numerical analysis is conducted using the finite volume-based ANSYS Fluent 2021/R2 commercial solver. The Pressure-Implicit with Splitting of Operators (PISO) algorithm is used to couple pressure and velocity. The PRESTO! scheme is applied for the discretization of the pressure equation, while a second-order upwind scheme is used for the discretization of momentum and energy equations.

2.3. Grid and time independence studies

Mesh size independence is essential for ensuring convergence and accuracy in numerical simulations and that the solution remains unaffected by variations in mesh discretization. For a discharge rate of 5C at an ambient temperature of 40 °C and a convective heat transfer coefficient of 20 W/m²·K using n-Docosane, grid

independence is evaluated with three element sizes: 1.25 mm, 1 mm, and 0.75 mm. The corresponding mesh counts for the battery with a PCM thickness of 3 mm are 46,632, 66,585, and 132,792, respectively, as illustrated in Figure 2(a). Minimal differences in the results led to the selection of a 0.75 mm element size as optimal for the PCM-integrated setup.

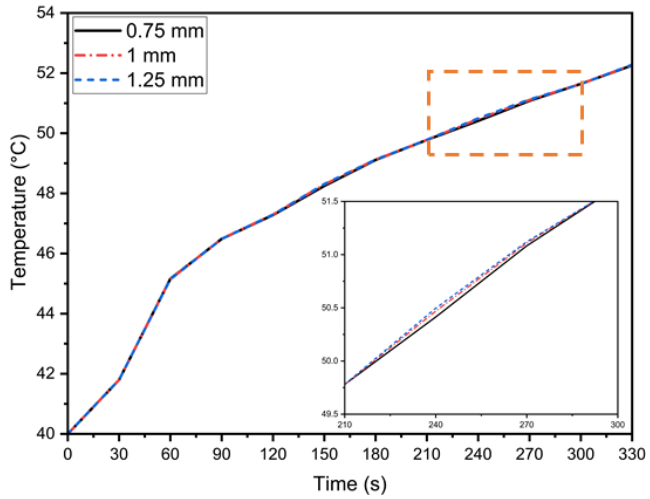

(a)

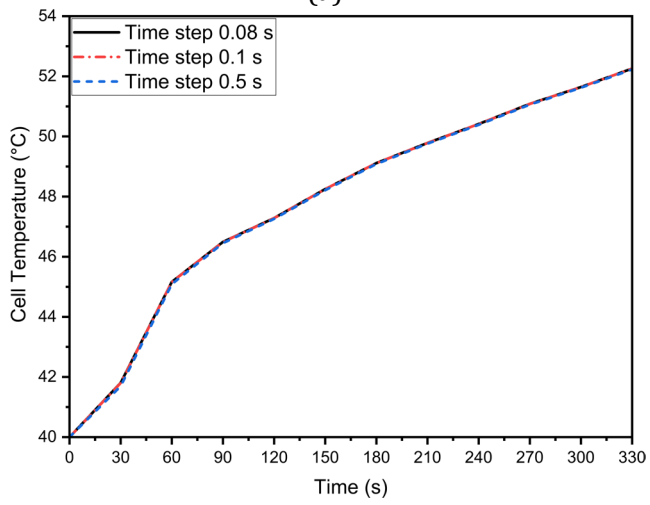

(b)

Figure 2. (a) Grid size independence study and (b) time step independence study.

Time step optimization is performed to balance computational efficiency and accuracy. Under the same conditions and using a 0.75 mm element size, Figure 2(b) displays three timesteps: 0.08 s, 0.1 s, and 0.5 s. The results showed negligible differences across these time steps, resulting in selecting a 0.5 s time step for the battery with PCM configurations.

2.4. Numerical Model Validation

The present numerical model is based on the NTGK model and is validated against the experimental study by Trimbake et al. [17] and the numerical analysis by Jithin et al. [13]. Both studies investigate a Samsung 26J 18650 2600 mAh battery pack in a 4S1P configuration. The experiments discharged the batteries at 2C (5.2 A) and 1C (2.6 A) using a 200 W electronic load, focusing on a 1C discharge scenario with h=5 W/m^2·K.

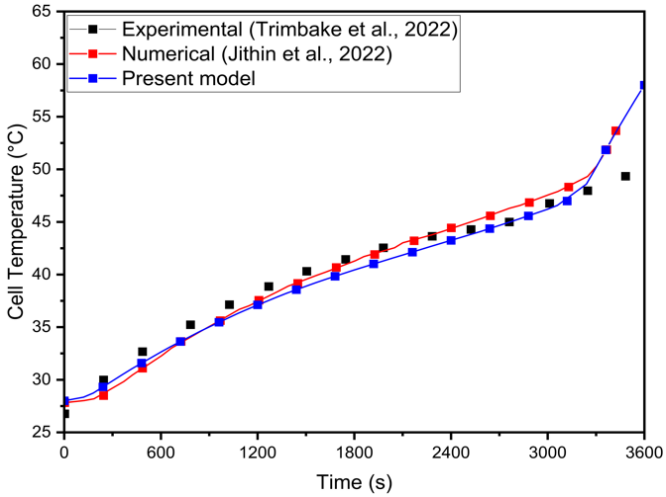

(a)

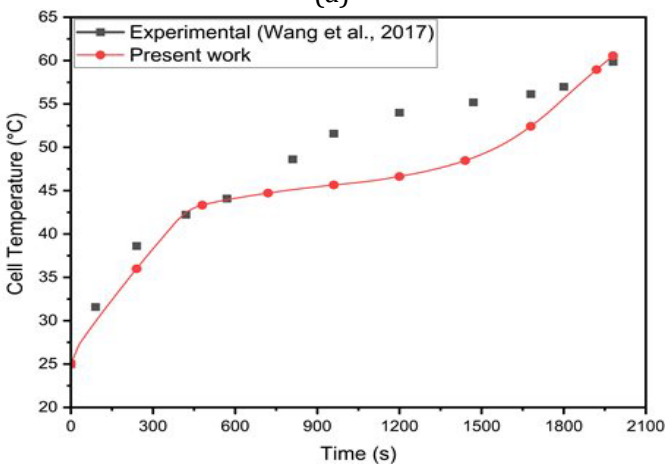

(b)

Figure 3. Model validation of (a) battery pack with experimental results [17], and numerical results [8], [13], (b) PCM and fins with experimental results [18].

Figure 3(a) compares the battery's cell temperature over time using experimental and numerical data. Temperature measurements reveal a distinct pattern: a rapid initial rise, a gradual increase, and a final spike, which is accurately predicted by the present numerical model. The numerical results closely match the experimental data, with maximum deviations of 11.48% and 2.95% compared to Trimbake et al. [17] and Jithin et al. [13], respectively.

The numerical model for a PCM-integrated battery in this study is validated against the experimental results of Wang et al. [18], who investigated the thermal behavior of a cylindrical 18650 LIB encapsulated with composite paraffin. Their setup, featuring K-type thermocouples for temperature measurement, evaluated the PCM's melting process and its impact on battery temperature regulation. Figure 3 (b) shows the maximum and average deviations between numerical and experimental results as 13.6% and 5.4%, respectively, attributed to unreported heater properties in the literature. This validation highlights the model's accuracy in simulating thermal dynamics, confirming its reliability for LIB thermal management applications.

3. Results and Discussion

3.1 Effect of PCM Thickness

In thermal management systems for lithium-ion batteries, selecting the optimal thickness of PCMs is crucial to balance temperature control and material efficiency. Figure 4 presents the temperature profiles for both the cell and the PCM during a 5C discharging cycle at an ambient temperature of 40 °C, comparing PCM thicknesses of 3 mm and 4 mm. The materials analyzed are n-Heneicosane, OM42, and n-Docosane, with h=20 W/m^2·K. The results in Figure 4 (a) reveal that the maximum cell temperatures at the end of the discharging process of 330 s reach 53.19 °C, 55.31 °C, and 52.23 °C for the 3 mm thick layers of n-Heneicosane, OM42, and n-Docosane, respectively. When the PCM thickness is increased to 4 mm, the maximum cell temperatures are slightly reduced to 51.94 °C, 53.16 °C, and 51.55 °C for the respective materials. This reduction indicates that thicker PCM layers absorb more heat during the high-rate discharging cycle, thus keeping the cell temperature within the target operational range. Similarly, the maximum PCM temperatures, as seen in Figure 4 (a), reach 47.13 °C, 50.72 °C, and 46.20 °C for the 3 mm thick layers of n-Heneicosane, OM42, and n-Docosane, respectively. With 4 mm thick PCM layers, these temperatures decrease to 43.92 °C, 45.57 °C, and 44.67 °C, respectively. Figure 4 (b) shows the liquid fraction of the PCMs over time, highlighting the extent of melting during the discharging cycle. At t = 0 s, the n-Heneicosane is in the partially melted state as its melting temperature is below the ambient temperature of 40 °C, whereas OM42 and n-Docosane are in the solid phase. The maximum melting fractions for the 3 mm thick PCMs are 98.01%, 100%, and 93.04%, respectively, for n-Heneicosane, OM42, and n-Docosane. In contrast, the corresponding 4 mm thick PCMs show significantly lower melting fractions of 43.92%, 45.57%, and 44.67% at 330 s.

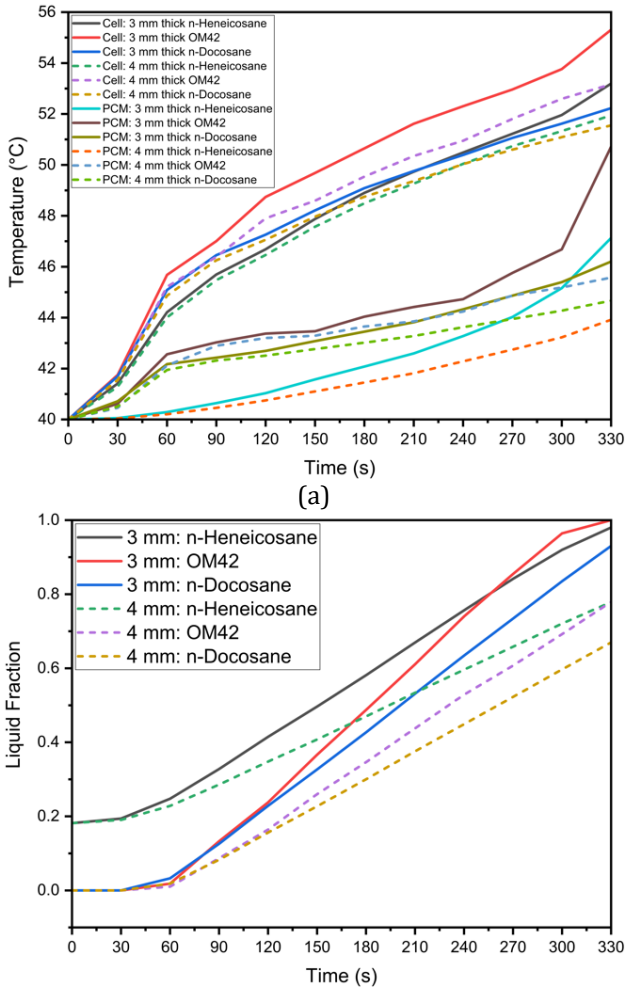

Figure 4. Effect of PCM thickness during a 5C discharging cycle at 40 °C ambient temperature and h=20 W/m^2·K, (a) cell and PCM temperature profiles, (b) liquid fraction profiles

Therefore, the OM42 shows a higher melt fraction at the end of the discharging process of 330 s owing to a lower single melting temperature (43 °C) and the lowest latent heat of fusion (~40% lower than n-Heneicosane) among the three PCMs, leading to earlier melting. Furthermore, the OM42 temperature during discharging remains consistently higher than n-Heneicosane and n-Docosane as the melting initiates at a higher temperature. It can be noted that n-Heneicosane and n-Docosane melt over a range of temperatures, and the melting starts earlier than OM42. Hence, the cell temperature for OM42 is significantly higher compared to the other two PCMs. However, it is further observed that the cell temperature

for n-Heneicosane is higher compared to that of n-Docosane at 330 s, whereas the opposite trend is observed at 180 s for both the cases of 3 mm and 4 mm PCM thicknesses. This is because n-Heneicosane has a lower completion melting temperature of 43.6 °C than n-Docosane (44.7 °C). As a result, n-Heneicosane melts completely slightly before 330 s, leading to higher cell temperature. However, at 180 s, the PCM temperature of n-Heneicosane is lower than that of n-Docosane, as the initiation of melting of n-Heneicosane is significantly earlier (39.2 °C) compared to n-Docosane (42.1 °C), which maintains the cell temperature lower, as can be seen in Figure 4(a). This can also be seen from the temperature contour plots presented later.

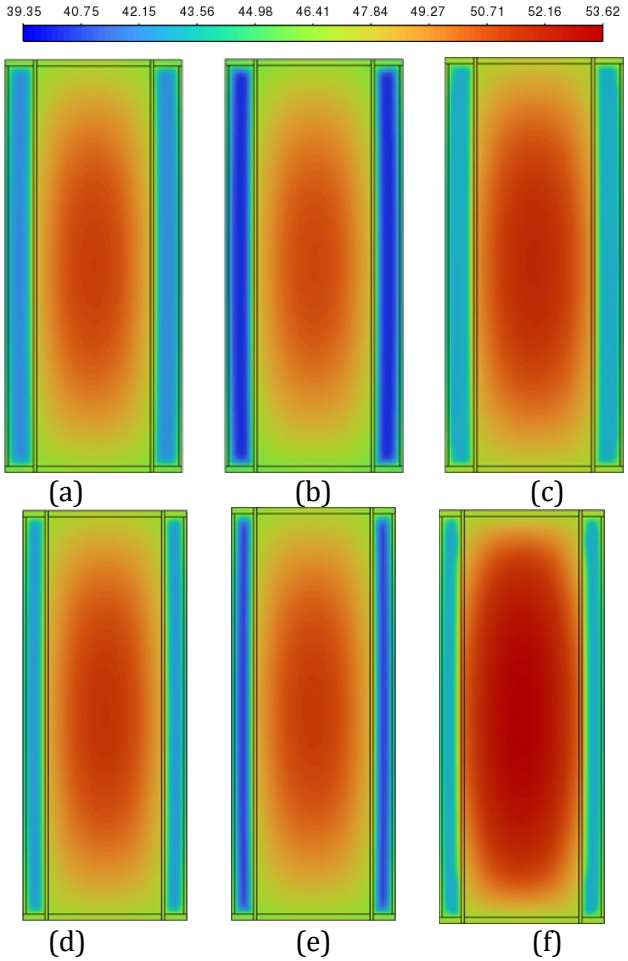

Figure 5. Contours of temperature (°C) for 5C discharging cycle at 40 °C ambient temperature and h=20 W/m^2·K (a), (d) n-Docosane, (b), (e) n-Heneicosane, and (c), (f) OM42 for 4 mm and 3 mm thickness of PCMs at 180 s.

Figures 5 and 6 provide a detailed analysis of the PCM and battery performance using contour plots for temperature and velocity vectors, respectively, on the cross-sectional plane B-B` at 180 s. These figures compare PCM thicknesses of 3 mm and 4 mm during a 5C discharging cycle at a 40 °C ambient temperature with a convective heat transfer coefficient of h=20 W/m^2·K. Figure 5 illustrates temperature contours, showing that the 4 mm PCM layer achieves greater thermal uniformity (maximum temperature difference for OM42 = 9.02 °C) as the PCM melts partially compared to the 3 mm layer, which exhibits higher thermal gradients due (maximum temperature difference for OM42 = 10.62 °C) to the almost complete melting of PCM. This improved uniformity is attributed to the higher heat absorption capacity of the thicker PCM.

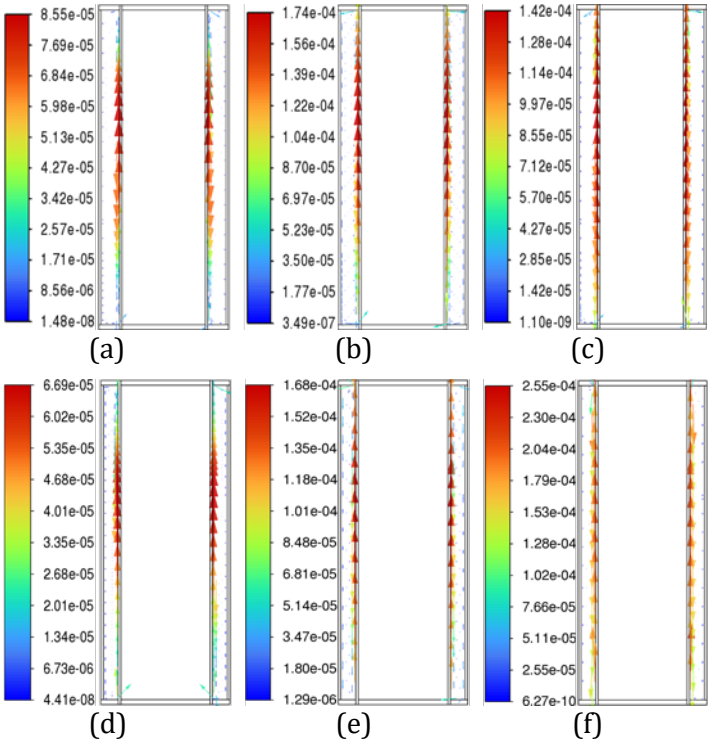

Figure 6. Velocity vector (m/s) for 5C discharging cycle at 40 °C ambient temperature and h=20 W/m^2·K (a), (d) n-Docosane, (b), (e) n-Heneicosane, and (c), (f) OM42 for 4 mm and 3 mm thickness of PCMs respectively at 180 s.

Figure 6 depicts velocity vector fields, highlighting that the fluid velocity within the 4 mm PCM is lower as PCM in 4 mm thickness melts less, whereas the 3 mm PCM shows higher velocity magnitudes, reflecting more active phase change dynamics due to a higher amount PCM in the molten state. These observations underline the trade-off between thermal uniformity and latent heat utilization, with the 4 mm PCM providing better thermal regulation and the 3 mm PCM demonstrating higher phase change efficiency. The 4 mm PCM layers of n-Heneicosane, OM42, and n-Docosane exhibit lower

internal fluid velocities during discharge, as shown in Figure 6, indicating limited convection from partial melting. This reduced flow retains a low liquid fraction, reducing convection-driven heat transfer. In contrast, the 3 mm layers show complete melting, resulting in higher fluid motion and steeper temperature gradients, as illustrated in Figure 5. This suggests that thicker PCM layers are more effective at temperature control, but do not fully utilize their latent heat capacity for the 5C discharging rate. Considering the balance between temperature regulation and effective material utilization, the 3 mm PCM thickness emerges as the optimal choice across all three materials.

3.2 Effect of ambient temperatures on PCM with cell

The performance of PCMs in managing the thermal behaviour of LIBs is highly sensitive to changes in ambient temperature. Figure 7 presents the effect of ambient temperature on the thermal management performance of n-Heneicosane, OM42, and n-Docosane during a 5C discharging cycle, with a PCM thickness of 3 mm and h=20 W/m^2·K. In Figure 7(a), the cell temperature profiles indicate that as the ambient temperature increases from 30 °C to 40 °C, the maximum cell temperature rises for all PCMs. OM42 results in the highest cell temperatures across all ambient conditions, as the melting of the PCM occurs at 43 °C. For ambient temperatures of 30 °C and 35 °C, the maximum cell temperature is consistently higher for n-Docosane than n-Heneicosane. The n-Heneicosane has the highest latent heat of fusion and the lowest initiation of melting temperature, which causes longer stabilization time at the lower PCM temperature. However, for ambient temperatures of 40 °C, the maximum cell temperature is higher for n-Heneicosane at 330 s, whereas it is lower at 180 s. This can be attributed to the earlier completion of melting of partially melted n-Heneicosane at an ambient temperature of 40 °C, leading to a rapid rise in the cell temperature at around 270 s.

Figures 7(b) and 7(c) show the corresponding PCM temperature profiles and the liquid fraction variation with time. The maximum PCM temperature and liquid fraction of PCM also increase with rising ambient temperatures. As observed, the PCM temperature and liquid fraction are highest for OM42 for all the ambient temperatures. Similar to the maximum cell temperature, the PCM temperature and liquid fraction follow the same variation for the three PCMs chosen in this study for all the ambient temperatures.

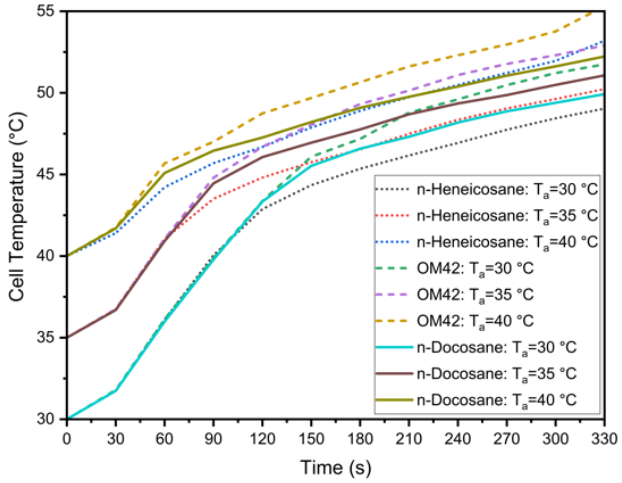

(a)

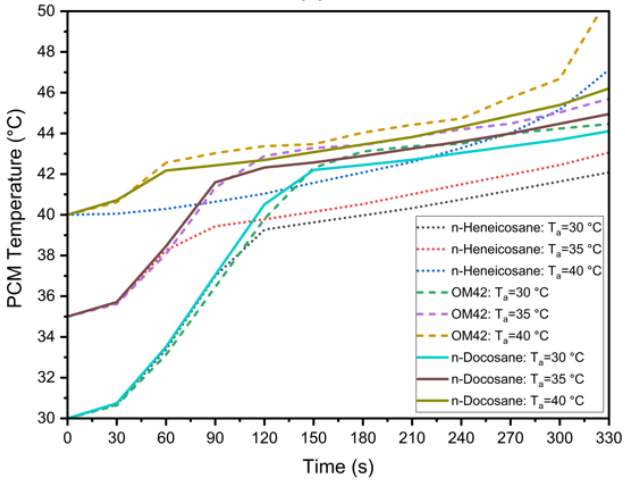

(b)

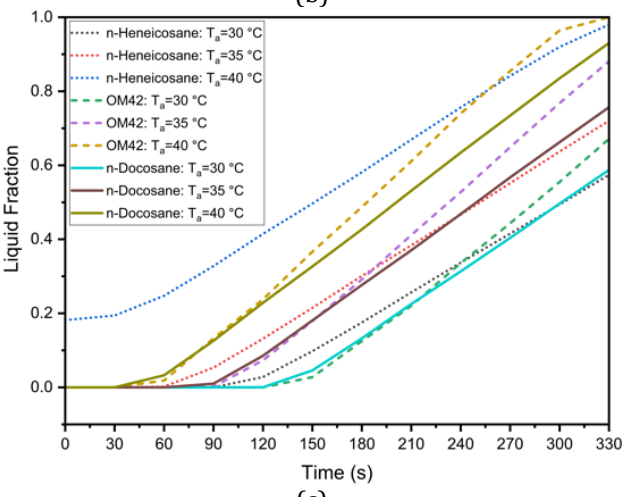

(c)

Figure 7. Effect of ambient temperatures for 3 mm PCM thickness and h=20 W/m^2·K, (a) cell temperature profiles, (b) PCM temperature profiles, (c) liquid fraction of PCMs.

Figures 8 and 9 illustrate temperature and velocity vector contours, respectively, on the cross-sectional plane B-B' for ambient temperatures of 30 °C and 35 °C

during a 5C discharging cycle with a 3 mm PCM thickness and a convective heat transfer coefficient of h=20 W/m^2·K. Figure 8 shows the temperature contours, where the temperature of the battery has increased significantly at 35 °C compared to 30 °C, resulting in higher temperature gradients across the PCM and battery.

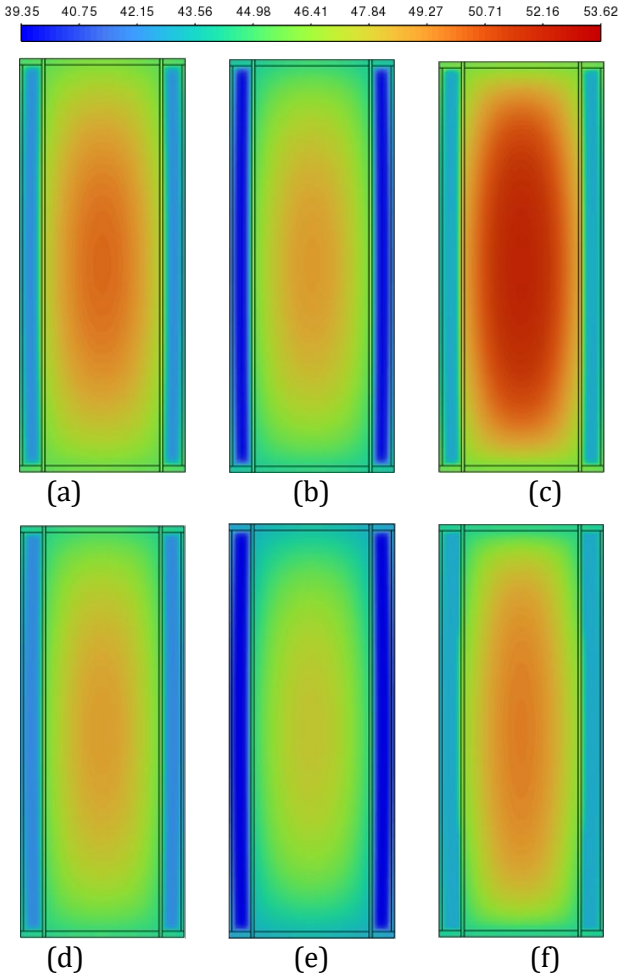

Figure 8. Contours of temperature (°C) for 5C discharging cycle at h=20 W/m^2·K for 3 mm thickness of PCMs (a), (d) n-Docosane, (b), (e) n-Heneicosane, and (c), (f) OM42 for 35 °C and 30 °C ambient temperature at 180 s.

The maximum melting fraction reaches 57.41%, 72.02%, and 98.01% for n-Heneicosane; 67.13%, 88.09%, and 100% for OM42; and 58.73%, 75.70%, and 93.04% for n-Docosane at ambient temperatures of 30 °C, 35 °C, and 40 °C, respectively. As expected, higher ambient temperatures lead to greater PCM melting, with OM42 achieving complete melting at 40 °C, which correlates with its higher cell and PCM temperatures observed earlier. Among the PCMs tested, n-Docosane demonstrates the most consistent performance across the different ambient temperatures, maintaining lower cell and PCM temperatures under the most extreme conditions.

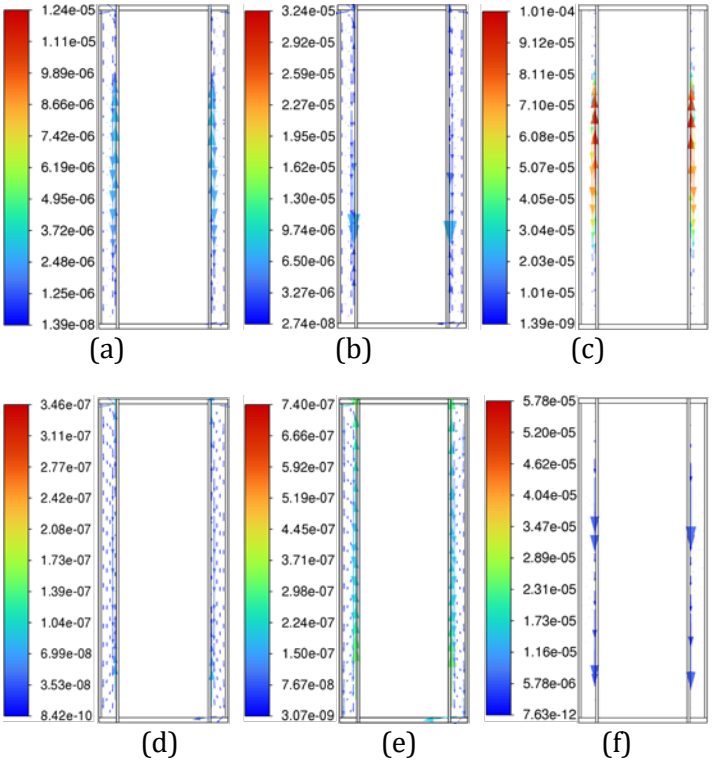

Figure 9. Velocity vector (m/s) for 5C discharging cycle at h=20 W/m^2·K for 3 mm thickness of PCMs (a), (d) n-Docosane, (b), (e) n-Heneicosane, and (c), (f) OM42 for 35 °C and 30 °C ambient temperature at 180 s.

Figure 9 presents velocity vector contours, demonstrating more dynamic fluid motion within the PCM at 35 °C, corresponding to accelerated phase transition processes due to higher thermal energy input. At an ambient temperature of 35 °C, the reduced temperature difference between the Li-ion battery and its surroundings lowers external heat dissipation, causing a larger fraction of heat stored in the PCMs of n-Heneicosane, OM42, and n-Docosane. This results in a rise in temperature gradients, which accelerates the melting process, as evidenced by the temperature contours in Figure 8. OM42, having a lower melting point and lower thermal diffusivity, melts rapidly due to thermal stratification, exhibiting higher velocity. In contrast, n-Docosane possesses higher latent heat and melts at a slower rate, distributing absorbed heat more evenly due to higher thermal diffusivity. These contrasting thermophysical properties account for the different velocity fields shown in Figure 9, where OM42 demonstrates higher liquid PCM motion and n-Docosane

maintains a comparatively lower magnitude velocity of liquid PCM. These results emphasize the impact of ambient temperature on the phase change behaviour and overall thermal performance of the PCM and battery system. OM42 exhibits the highest temperature rise, indicating a more significant phase change, which aligns with its higher melting fraction and the corresponding cell temperature results.

3.3 PCMs Thermal Performance at 35 °C

This study focuses on the thermal behaviour of PCMs near their melting points, specifically focusing on 35 °C, an ambient temperature common during summer in India. Figure 10 illustrates the thermal behaviour of n-Heneicosane, OM42, and n-Docosane during a 5C discharging cycle followed by a 1C charging cycle at an ambient temperature of 35 °C, with a PCM thickness of 3 mm and h=20 W/m^2·K during discharging, and h=50 and 100 W/m^2·K during charging. Figure 10(a) shows that the maximum cell temperatures during the 5C discharging cycle reach 50.23 °C, 52.90 °C, and 51.07 °C for n-Heneicosane, OM42, and n-Docosane, respectively, at 330 s, as explained above. The corresponding maximum PCM temperatures are 43.06 °C, 45.7 °C, and 44.95 °C at the end of discharging. Among these, OM42 exhibits the highest temperature rise at 330 s, indicating a more significant phase change and greater heat absorption than other PCMs. The lowest temperature. Figure 10(b) reveals the liquid fraction profiles at the end of the discharging cycle, where the maximum melting percentages are 72.02%, 88.09%, and 75.70% for n-Heneicosane, OM42, and n-Docosane, respectively. During the subsequent 1C charging process, the initial heat transfer coefficient of h=50 W/m^2·K proves inadequate for complete PCM solidification by the end of the cycle, leaving temperatures elevated. Thus, a higher coefficient of h=100 W/m^2·K results in a sudden drop in temperature as the PCMs fully solidify at approximately 1200 s, 780 s, and 720 s for n-Heneicosane, OM42 and n-Docosane, respectively. The shorter solidification time for n-Docosane can be attributed to higher thermal diffusivity and the relatively lower melt fraction at the end of the melting process of the PCM, as the mode of heat transfer during the solidification of PCM is dominated by conduction. n-Heneicosane takes longer to solidify due to its highest latent heat of fusion. Interestingly, OM42 has a higher solidification rate during the 1C charging as it has the lowest latent heat of fusion. This rapid solidification underscores the effectiveness of a higher heat transfer coefficient in hastening the thermal recovery of the PCM. It can be concluded that n-Docosane emerges as the optimum PCM for ensuring both effective heat management and rapid thermal recovery in lithium-ion battery systems operating under these conditions.

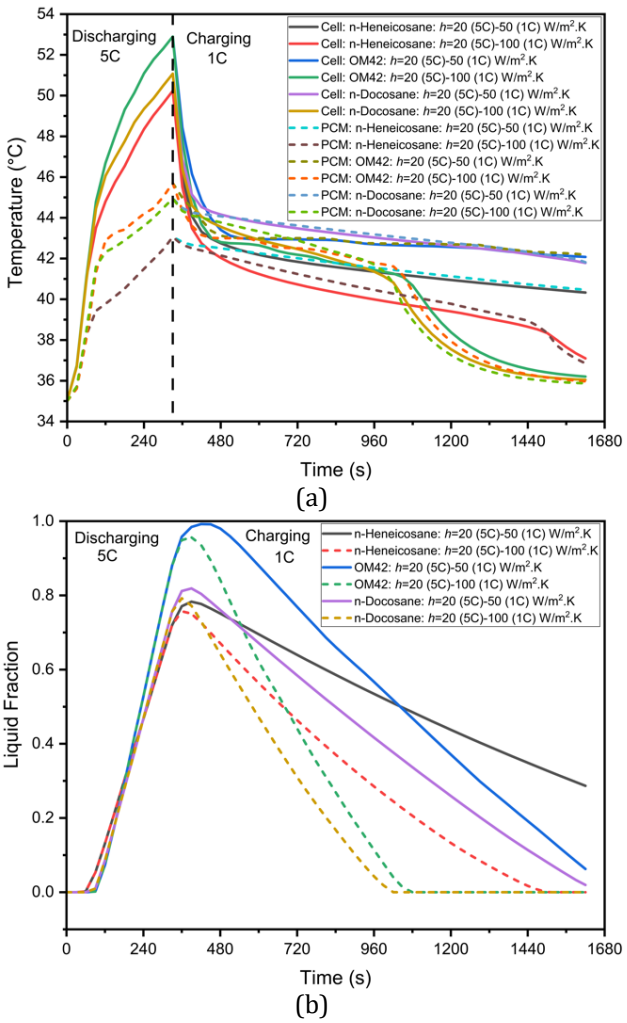

Figure 10. Temperature and liquid fraction profiles during a 5C discharging and 1C charging cycle with 3 mm PCM thickness and h=20 W/m^2·K for discharging and h=50 and 100 W/m^2·K for charging, (a) cell and PCM temperature profiles, (b) liquid fraction of PCMs.

3.4 Solidification at Harsh Conditions (40 °C, n-Docosane)

This section examines n-Docosane's solidification efficiency under extreme conditions at 40 °C, which is critical for maintaining battery performance during rapid cycles. Figure 11 illustrates the thermal behaviour and phase change characteristics of n-Docosane during a 5C discharging cycle followed by a 1C charging cycle under harsh ambient conditions of 40 °C. Figure 11(a) shows that the maximum cell temperature reaches 52.23

°C, while the maximum PCM temperature reaches 46.20 °C at the end of the 5C discharging cycle. The melt fraction of n-Docosane is 93.04%, as shown in Figure 11(b).

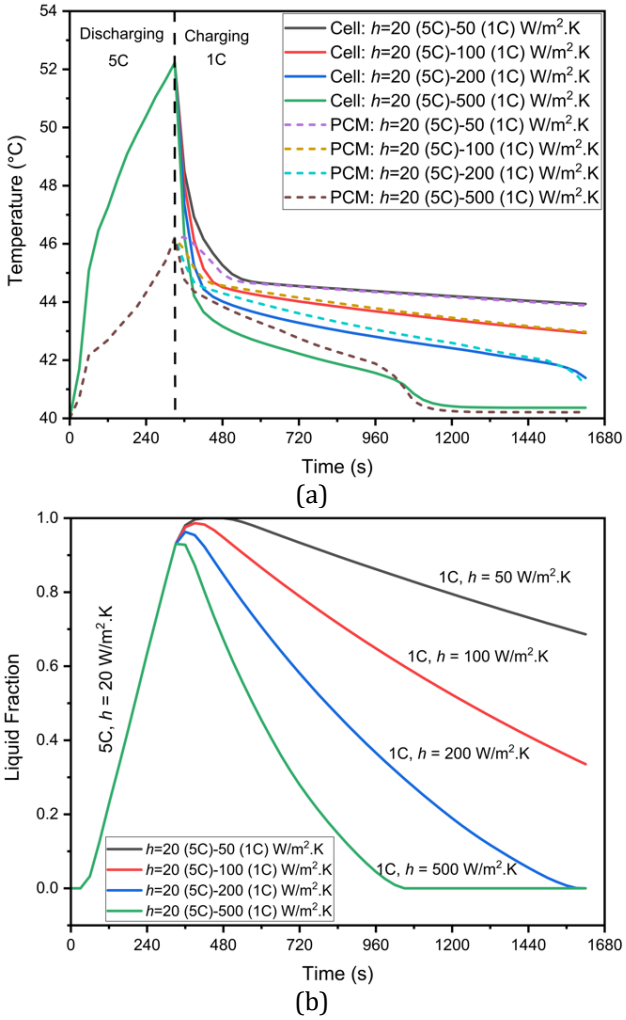

Figure 11. (a) Cell and PCM temperature, (b) liquid fraction, profiles during a 5C discharging and 1C charging cycle with 3 mm n-Docosane and h=20 W/m²·K for discharging and various heat transfer coefficients for charging.

Following the discharging phase, the 1C charging process begins, and Figure 11(a) demonstrates the usefulness of a higher heat transfer coefficient in achieving complete solidification. At h=50 and 100 W/m²·K, the PCM does not fully solidify at the end of the charging cycle, as indicated by the higher temperatures and liquid fraction seen in Figure 11(b). Consequently, higher heat transfer coefficients of h=200 and 500 W/m²·K are applied, resulting in rapid temperature decrease and complete solidification of n-Docosane. The time required for solidification is significantly reduced, with h = 200 W/m²·K achieving solidification in 1290 s and h = 500 W/m²·K in 750 s. This outcome demonstrates the importance of optimizing convective heat transfer in maintaining effective thermal management under extreme conditions.

4. Conclusion

This study investigated the thermal management of lithium-ion batteries using PCMs under different conditions, focusing on PCM thickness, ambient temperature, and convective heat transfer coefficients. The objective is to determine the optimal PCM configuration for maintaining safe battery temperatures during high-rate discharging and charging cycles, particularly under challenging conditions. Increasing the PCM thickness from 3 mm to 4 mm results in lower maximum cell temperatures. However, the 4 mm thickness shows reduced PCM utilization, making 3 mm the optimal thickness for balancing temperature control and PCM efficiency. Ambient temperatures between 30 °C and 40 °C directly affect PCM and cell temperatures. The highest cell temperature observed for OM42 at 40 °C is 55.31 °C, indicating a decreased heat transfer performance with rising ambient temperatures despite complete PCM melting. In contrast, n-Docosane demonstrates superior thermal regulation and complete solidification, making it more suitable for these conditions. At a typical ambient temperature of 35 °C in India, n-Docosane maintains lower peak temperatures and solidifies more efficiently during charging. Under extreme conditions of 40 °C, n-Docosane requires increased convective heat transfer coefficients to achieve complete solidification during the charging cycle. At a coefficient of 500 W/m²·K, the solidification of PCM is completed within 750 s, highlighting the importance of enhanced cooling for maintaining battery performance. This study identified n-Docosane as the most effective PCM for lithium-ion battery thermal management across various conditions, providing reliable temperature regulation and efficient phase transitions.

References

[1] M. Mashayekhi, "Factors Influencing the Diffusion of Battery Electric Vehicles in Urban Areas," Ryerson University Library and Archives, Jun. 2021.

[2] P. K. Nayak, E. M. Erickson, F. Schipper, T. R. Penki, N. Munichandraiah, P. Adelhelm, H. Sclar, F. Amalraj, B. Markovsky and D. Aurbach, "Review on Challenges and Recent Advances in the

Electrochemical Performance of High Capacity Li and MnRich Cathode Materials for LiIon Batteries," Adv. Energy Mater., vol. 8, no. 8, Dec. 2017.

[3] J. Xu, Y. Chen, and L. Dai, "Efficiently photo-charging lithium-ion battery by perovskite solar cell," Nat. Commun., vol. 6, no. 1, Aug. 2015.

[4] S. K. Jung, H. Kim, M. G. Cho, S. P. Cho, B. Lee, H. Kim, Y. U. Park, J. Hong, K. Y. Park, G. Yoon, W. M. Seong, Y. Cho, M. H. Oh, H. Kim, H. Gwon, I. Hwang, T. Hyeong, W. S. Yoon and K. Kang, "Lithium-free transition metal monoxides for positive electrodes in lithium-ion batteries," Nat. Energy, vol. 2, no. 2, Jan. 2017.

[5] B. Karmkar, R. Mokal, S. Landge, and B. Jadhav, "Design and Implement a BTMS using Phase Change Material - A Review," Int. J. Res. Appl. Sci. Eng. Technol., vol. 12, no. 5, pp. 4249–4253, May 2024.

[6] L. Song, "Thermal Performance Analysis of the Battery Thermal Management Using Phase Change Material," OALib, vol. 05, no. 12, pp. 1–5, 2018.

[7] C. W. Zhang, S. R. Chen, H. B. Gao, K. J. Xu, Z. Xia, and S. T. Li, "Study of Thermal Management System Using Composite Phase Change Materials and Thermoelectric Cooling Sheet for Power Battery Pack," Energies, vol. 12, no. 10, p. 1937, May 2019.

[8] V. A. Wagh and S. K. Saha, "Optimizing extended fin design and heat transfer coefficient for improved heat transfer and PCM recover time in thermal management of batteries," Appl. Therm. Eng., vol. 255, p. 123964, Oct. 2024, doi: 10.1016/j.applthermaleng.2024.123964.

[9] S. Li, Y. Cheng, Q. Shen, C. Wang, C. Peng, and G. Yang, "Numerical analysis on the thermal management of phase change material with fins for lithium-ion batteries," Int. J. Numer. Methods Heat Amp Fluid Flow, vol. 34, no. 3, pp. 1170–1188, Dec. 2023.

[10] A. Angani, E. Kim, and K. Shin, "Improvement of Thermal Performance of Electric Vehicle Battery Pack with Phase-change Material," Sens. Mater., vol. 32, no. 5, p. 1609, May 2020.

[11] T. Talluri, T. H. Kim, and K. J. Shin, "Analysis of a Battery Pack with a Phase Change Material for the Extreme Temperature Conditions of an Electrical Vehicle," Energies, vol. 13, no. 3, p. 507, Jan. 2020.

[12] "Sony: Lithium Ion Rechargeable Batteries (Wayback Machine)." [Online]. Available: https://web.archive.org/web/20090411024100/http://www.sony.com.cn/products/ed/battery/download.pdf

[13] K. V. Jithin and P. K. Rajesh, "Numerical analysis of single-phase liquid immersion cooling for lithium-ion battery thermal management using different dielectric fluids," Int. J. Heat Mass Transf., vol. 188, p. 122608, Jun. 2022, doi: 10.1016/j.ijheatmasstransfer.2022.122608.

[14] D. Velliadou, K. D. Antoniadis, A. N. Assimopoulou, M. J. Assael, M. C. M. Sequeira, and W. A. Wakeham, "Accurate Measurements of the Thermal Conductivity of n-Docosane, n-Tetracosane, 1,6-Hexanediol, and 1,8-Octanediol in the Solid and Liquid Phases," Int. J. Thermophys., vol. 44, no. 5, Apr. 2023, doi: 10.1007/s10765-023-03182-6.

[15] A. N. S. Y. S. Inc, "ANSYS fluent theory guide." 2020. [Online]. Available: https://www.ansys.com

[16] M. S. Patil, J. H. Seo, and M. Y. Lee, "A novel dielectric fluid immersion cooling technology for Li-ion battery thermal management," Energy Convers Manag, vol. 229, 2021, doi: 10.1016/j.enconman.2020.113715.

[17] A. Trimbake, C. P. Singh, and S. Krishnan, "Mineral oil immersion cooling of lithium-ion batteries: an experimental investigation," J Electrochem Energy Convers Storage, vol. 19, no. 2, 2022, doi: 10.1115/1.4052094.

[18] Wang Z, Zhang H, Xia X., "Experimental investigation on the thermal behavior of cylindrical battery with composite paraffin and fin structure," Int J Heat Mass Transf 2017;109:958–70.